Soft Matter

PAPER

Check for updates

Aggregation of amphiphilic nanocubes in equilibrium and under shear

Takahiro Yokoyama, [ID] [a] Yusei Kobayashi, [ID] [b] Noriyoshi Arai [ID] [a] and Arash Nikoubashman [ID] ★[acde]

We investigate the self-assembly of amphiphilic nanocubes into finite-sized aggregates in equilibrium and under shear, using molecular dynamics (MD) simulations and kinetic Monte Carlo (KMC) calculations. These patchy nanoparticles combine both interaction and shape anisotropy, making them valuable models for studying folded proteins and DNA-functionalized nanoparticles. The nanocubes can self-assemble into various finite-sized aggregates ranging from rods to self-avoiding random walks, depending on the number and placement of the hydrophobic faces. Our study focuses on suspensions containing multi- and one-patch cubes, with their ratio systematically varied. When the binding energy is comparable to the thermal energy, the aggregates consist of only few cubes that spontaneously associate/dissociate. However, highly stable aggregates emerge when the binding energy exceeds the thermal energy. Generally, the mean aggregation number of the self-assembled clusters increases with the number of hydrophobic faces and decreases with increasing fraction of one-patch cubes. In sheared suspensions, the more frequent collisions between nanocube clusters lead to faster aggregation dynamics but also to smaller terminal steady-state mean cluster sizes. The results from the MD and KMC simulations are in excellent agreement for all investigated two-patch cases, whereas the three-patch cubes form systematically smaller clusters in the MD simulations compared to the KMC calculations due to finite-size effects and slow aggregation kinetics. By analyzing the rate kernels, we are able to identify the primary mechanisms responsible for (shear-induced) cluster growth and breakup. This understanding allows us to tune nanoparticle and process parameters to achieve desired cluster sizes and shapes.

[a] Department of Mechanical Engineering, Keio University, 223-8522 Yokohama, Japan. E-mail: anikouba@ipfdd.de

[b] Faculty of Mechanical Engineering, Kyoto Institute of Technology, Matsugasaki, Sakyo-ku, Kyoto 606-8585, Japan

[c] Institute of Physics, Johannes Gutenberg University Mainz, Staudingerweg 7, 55128 Mainz, Germany

[d] Leibniz-Institut für Polymerforschung Dresden e.V., Hohe Straße 6, 01069 Dresden, Germany

[e] Institut für Theoretische Physik, Technische Universität Dresden, 01069 Dresden, Germany

I. Introduction

The assembly of nanoparticles into superstructures can be directed by patterning their surface with small functional "patches",[1–4] thereby introducing highly localized interactions with controlled valence. In contrast to isotropic nanoparticles, the interactions between patchy particles are highly directional, which enables the formation of finite-sized aggregates such as micelles and vesicles[4–8] as well as system-spanning gel-like networks[9,10] at thermodynamic equilibrium. This large spectrum of feasible superstructures and the ability to tune the (surface) chemistry of the individual particles facilitates a wide

range of applications, including bio-imaging and targeted drug delivery,[11,12] interfacial stabilization,[13–16] and catalysis.[17,18]

The self-assembly behavior of nanoparticles also depends on their shape,[3] thus providing an additional handle for controlling their structure formation. Natural particles cover a diverse range of shapes, including rod-like tobacco mosaic viruses[19,20] and gibbsite platelets,[21] which have inspired the development of experimental synthesis methods that can produce a variety of non-spherical nanoparticles.[2–4] Among these, cubic nanoparticles are particularly interesting due to their simple non-spherical geometry and space-filling properties.[22–25] Nanometer-sized cubes exhibit interesting material properties, which can differ strongly from their bulk counterparts because of finite-size and surface effects. For example, hematite nanocubes demonstrate superparamagnetic performance at room temperature,[26] while Au/Ag/Au core–shell–shell nanocubes combine the strong plasmonic properties of silver with the stable and functional surface chemistry of gold.[27] Perovskites based on, *e.g.*, Cs–PB–X, can also form cubic nanocrystals, which exhibit outstanding optical properties such as color-pure photoluminescence, making them promising low-cost optoelectronics components.[28]

The combination of shape and interaction anisotropy provides a powerful handle to control self-assembly on the microscopic level and the resulting (macroscopic) materials properties.[3,29–31] However, in practice it is often challenging to selectively modify the surfaces of nanocubes using bottom-up strategies, as typically all sides have the same surface chemistry. One promising pathway for creating nanocubes with patterned surfaces is DNA origami,[32–34] as demonstrated experimentally by Scheible *et al.*[35] Alternatively, the sequence of a protein can be designed such that it folds into a cube-shaped tertiary structure with highly specific interactions on its exposed surfaces, thus resembling a patchy particle;[36,37] for example, Du *et al.* recently engineered L-rhamnulose-1-phosphate proteins with histidine-mediated interactions, which fold into cube-shaped building blocks that can spontaneously self-assemble into supramolecular structures like nanoribbons or double-helical structures, depending on the pH of the buffer solution.[38]

Evidently, nanocubes feature a rich self-assembly behavior, which depends on, *e.g.*, their concentration and inter-particle interactions. Systematically exploring this vast parameter space is, however, challenging for experiments alone, as it requires the time- and resource-intensive particle synthesis and variation of many parameters. Computer simulations are ideally suited for this task, as they provide direct control over the particle properties and allow for efficiently exploring parameter space. In a recent article,[29] we studied through simulations the equilibrium self-assembly of amphiphilic cubes in the limit of non-reversible aggregation, finding elongated rod-like structures and tightly packed aggregates, depending on the number and arrangement of the hydrophobic faces on the cubes. In this work, we investigate in more detail the structure formation of multi-patch cubes at finite temperatures, finding extremely slow self-assembly dynamics in some cases due to the gradual recombination of the aggregates. We further simulate suspensions under shear flow, which exhibit accelerated assembly dynamics and shear-induced breakup at sufficiently high shear rates.

II. Model and methods

We specifically investigate binary mixtures of amphiphilic nanocubes, where a fraction f of the cubes have either two or three hydrophobic faces, while the remaining cubes have only one hydrophobic face. Although there are 6, 15, and 20 different possibilities to place the hydrophobic patches on the one-, two-, and three-patch cubes, respectively, only a small subset of patch arrangements are geometrically distinct, as shown in Fig. 1.[29] In the following, we refer to the two different realizations as type I and type II, respectively, as indicated in Fig. 1. We consider monodisperse suspensions, where all cubes have the same edge length d. This simplification is reasonable given that experimentally synthesized nanocubes[27,39–41] and folded proteins[38] typically have narrow size distributions. To examine the self-assembly of the nanocubes into finite-sized aggregates,
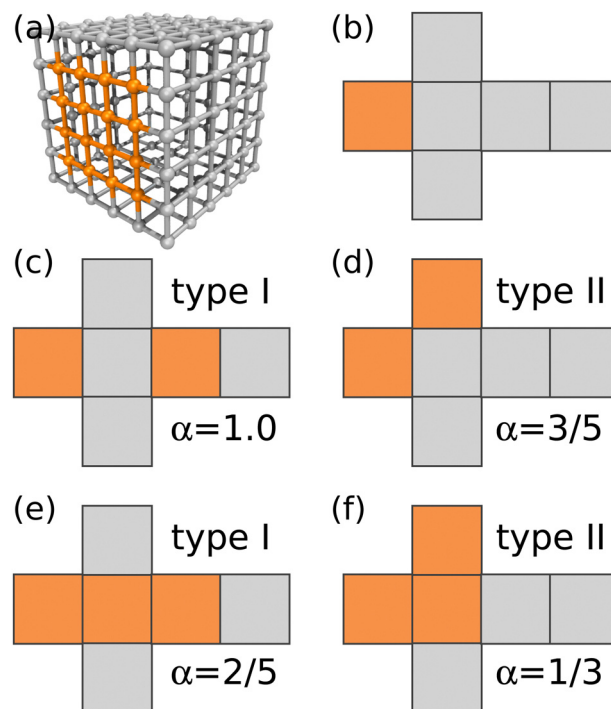

Fig. 1 (a) Discrete particle model of a terminal one-patch nanocube with diameter $d = 5a_v$. Vertex particles and bonds between nearest neighbors are shown, whereas diametric bonds have been omitted for clarity. (b)–(f) Unfolded representations of one-patch, two-patch, and three-patch cubes, including scaling exponent α used in the KMC simulations. In all panels, hydrophilic patches are colored in gray and hydrophobic ones in orange. Snapshot rendered using Visual Molecular Dynamics (version 1.9.3).[42]

we focus on nanoparticle volume fractions ϕ well below the freezing transition of hard cubes ($\phi_f \approx 0.5$).[23] We use molecular dynamics (MD) simulations with a discrete mesh model and rejection-free Kinetic Monte Carlo (KMC) calculations, which are described in detail in Sections II A and II B, respectively.

A. Molecular simulation

The MD simulations use a discrete particle model for the nanocubes,[29,43] which consist of N_v vertex particles of diameter a_v and mass m_v, arranged on a quadratic lattice on the cube surface [see Fig. 1(a)]. To maintain a (nearly) rigid nanoparticle shape, the vertex particles are connected with their nearest neighbor and with their diametrically opposite counterpart through a harmonic potential

$$U_b(r) = \frac{k}{2}(r - r_0)^2, \qquad (1)$$

where r and r_0 are the actual and desired distance between two bonded vertex particles, respectively. The spring constant is set to $k = 5000\ k_B T/a_v^2$,[29,43,44] with Boltzmann's constant k_B and temperature T. We chose a cube diameter of $d = 5a_v$ with lattice spacing $5/6a_v$, resulting in $N_v = 152$ vertex particles per nanocube. The mass of a nanocube is then $m = N_v m_v$. Each hydrophobic face consists of 16 vertex particles [see Fig. 1(a)], and the solvent-mediated attraction between them is modeled through

a pairwise Lennard-Jones (LJ) potential acting on the hydrophobic vertex particles

$$U_{LJ}(r) = \begin{cases} 4\varepsilon\left[(a_v/r)^{12} - (a_v/r)^6\right], & r \leq r_{cut}, \\ 0, & r > r_{cut} \end{cases} \quad (2)$$

with interaction strength ε and cutoff radius $r_{cut} = 3a_v$. Excluded volume interactions between hydrophilic vertex particles and between hydrophilic and hydrophobic vertex particles are modeled using the purely repulsive Weeks–Chandler–Andersen (WCA) potential[45]

$$U(r) = \begin{cases} U_{LJ}(r) + \varepsilon, & r \leq 2^{1/6} a_v \\ 0, & r > 2^{1/6} a_v \end{cases}. \quad (3)$$

Initial configurations are generated by placing N randomly oriented nanocubes at random positions without overlap in a cubic simulation box with edge length $80a_v = 16d$ and volume $V = (16d)^3$. The MD simulations are performed at nanocube volume fractions $\phi \equiv Nd^3/V = 0.014$ (58), 0.028 (115), 0.056 (230), and 0.112 (459), where the numbers in parentheses denote the total number of nanocubes in the simulation box. The equations of motion are solved using a velocity Verlet integration scheme with time step $\Delta t = 0.005\tau$, $\tau = \sqrt{m_v a_v^2/\varepsilon}$ being the derived unit of time. Unless stated otherwise explicitly, the temperature is fixed to $T = \varepsilon/k_B$. Equilibrium simulations are performed using an implicit solvent and a Langevin thermostat with friction coefficient $\xi_v = m_v/\tau$. To study the impact of hydrodynamic interactions, we perform additional explicit-solvent simulations using the multi-particle collision dynamics (MPCD) technique.[46–48] Here, we use the same MPCD parameters as in our previous works on sheared suspensions of Janus colloids,[8,49] i.e., a solvent number density of $\rho_s = 10a_v^{-3}$, a collision angle of $130°$, and an MPCD timestep of $\Delta t_{MPCD} = 0.1\tau$, which results in a solvent viscosity of $\eta_s = 8.72\varepsilon\tau/a_v^3$. Shear simulations are also performed with an explicit solvent, using the reverse perturbation method,[50] where an externally imposed shear stress leads to the emergence of a triangular velocity profile. To determine the measurement uncertainty of our MD data, we have conducted three independent runs per state point. All simulations are performed for at least 10^9 time steps using the HOOMD-blue software package (v. 2.9.6).[51]

B. Kinetic Monte Carlo

We assume that the cubes are uniformly distributed in space, and that aggregation events are pairwise. The characteristic size L_i of an aggregate depends on its number of constituent cubes, M_i, and their arrangement (see Fig. 2). For example, two-patch cubes which have their hydrophobic faces on opposite sides (type I) form rod-shaped aggregates of length $L_i \simeq dM_i$, whereas the aggregated cubes follow a self-avoiding random walk with $L_i \simeq dM_i^{3/5}$ when their two hydrophobic patches lie on adjacent faces (type II).[29,52] To distinguish between these different structures, we define the characteristic aggregate size as $L_i = dM_i^\alpha$ with scaling exponent $1/3 \leq \alpha \leq 1$. In general, α decreases with increasing number of hydrophobic surfaces,
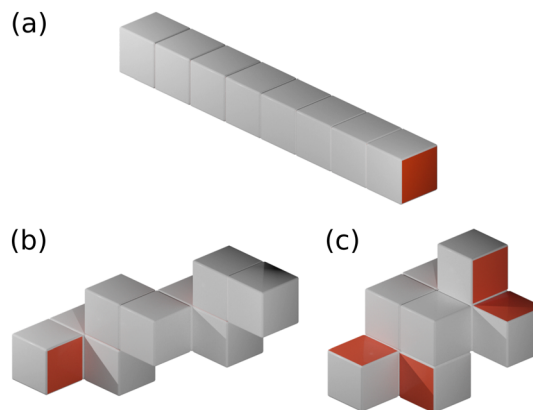

Fig. 2 Schematic renderings of $M = 8$ cubes self-assembled into (a) a rod ($\alpha = 1$), (b) a self-avoiding random walk ($\alpha = 3/5$), and (c) a compact configuration ($\alpha = 1/3$).

which is conceptually similar to the behavior of homopolymers in solution, where one finds $\alpha = 3/5$ and $\alpha = 1/3$ for good and bad solvent conditions, respectively.[52] One notable difference is, however, that the specific value of α also depends on the arrangement of patches on the cube surface. Like for polymers, these scaling exponents hold only for sufficiently large clusters (typically $M_i \gtrsim 5$),[29] with $\alpha = 1$ for $M_i \leq 2$ for all cases. For simplicity, we have not considered such size-dependent scaling exponents in our KMC model, which appears to be a reasonable approximation based on the overall good agreement with the MD simulations (see Section III). Further note that cluster configurations are generally possible for the type II two-patch cubes and both types of three-patch cubes, where a hydrophobic surface of one cube is occluded by a hydrophilic surface of another one. Our KMC model cannot capture such configurations, as it only stores the number and type of cubes in an aggregate, but not their specific connectivity. However, this effect is likely negligible, given that the typical cluster sizes in the MD simulations are almost indistinguishable for the different patch distributions (see Fig. 5(b) and 7(b) below).

Further, we neglect hydrodynamic interactions and crowding effects in our KMC model, so that the translational diffusion coefficient of an aggregate is given by $D_i = k_B T/(\xi M_i)$, with friction coefficient ξ. When hydrodynamic interactions are included, D_i becomes inversely proportional to the hydrodynamic size of the aggregate, which is not necessarily identical to its characteristic geometric size L_i (see, e.g., ref. 53 for rod-shaped clusters). For simplicity, we focus on systems without hydrodynamic interactions, and demonstrate briefly in Section III that the inclusion of hydrodynamic interactions only has a minor impact on the aggregation kinetics (static equilibrium properties, such as the cluster size distribution, are not affected at all).

In KMC, the system evolves through defined processes with known transition rates. At each time step, an event is chosen based on its probability, which is calculated as the ratio of the rate of the event to the sum of the rates of all possible events. The system and transition rates are then updated, and the time is advanced using $\Delta t = -\ln(u)/K_T$, where u is a uniformly
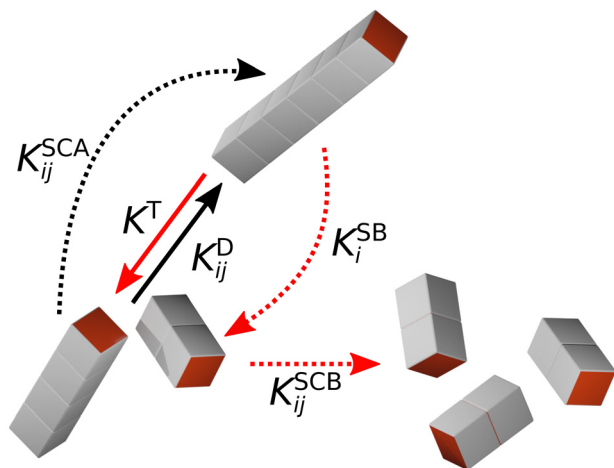
Fig. 3 Schematic representation of all aggregation/breakup events. Black and red arrows indicate cluster aggregation and breakup events, respectively, while shear-induced events are indicated by dashed arrows.

Fig. 4 Binding energy U_{bind} (left axis) and force F_{bind} (right axis) between two discretized hydrophobic cube surfaces at distance z. Inset: schematic representation of two hydrophobic cube faces in the discrete particle model at separation z.

distributed random number in the interval (0,1). This procedure causes the time evolution of the system to speed up as events become less likely, in contrast to the linear time evolution of MD simulations. In our previous KMC calculations,[29] we only considered the irreversible aggregation of one- and two-patch cubes into rod-shaped aggregates at rest. Here, we extend our KMC model to mixtures of one- and three-patch cubes and take into account five different aggregation/breakup events, which are schematically illustrated in Fig. 3:

1. The diffusion-driven aggregation of two clusters i and j is modeled using the Smoluchowski coagulation equation[54,55] with kernel

$$K_{ij}^{DA} = \frac{W_{ij}}{V}(L_i + L_j)(D_i + D_j). \quad (4)$$

The parameter W_{ij} controls the likelihood of two clusters i and j merging during a collision. In this study, we use $W_{ij} = W_i W_j$, where W_i and W_j are the area fraction of the exposed hydrophobic surface of clusters i and j, respectively. For example, a single three-patch cube has $W_i = 3/6$, whereas a dimer composed of one three-patch and one one-patch cube has $W_j = 2/10$, resulting in $W_{ij} = 1/10$. Note that we erroneously wrote $K_{ij}^{DA} \propto 1/W_{ij}$ in our previous article,[29] but used expression (4) for the actual KMC simulations.

2. Aggregates can also spontaneously break up, if the binding energy U_{bind} is finite. Assuming dissociation into two pieces and ignoring entropic contributions to the Helmholtz free energy of the system, we model this thermally induced cluster breakup *via* the kernel

$$K^{TB} = A\tau_D^{-1} \exp[-U_{bind}/(k_B T)], \quad (5)$$

where $\tau_D \equiv d^2/(6D_0)$ is the characteristic diffusion time of a single cube, and A and U_{bind} are model specific parameters. To facilitate the comparison between our KMC calculations and MD simulations, we determine U_{bind} by computing the potential energy acting between two hydrophobic faces of our discretized cube model [*cf.* Fig. 1(a)]. Fig. 4 shows U_{bind} and the
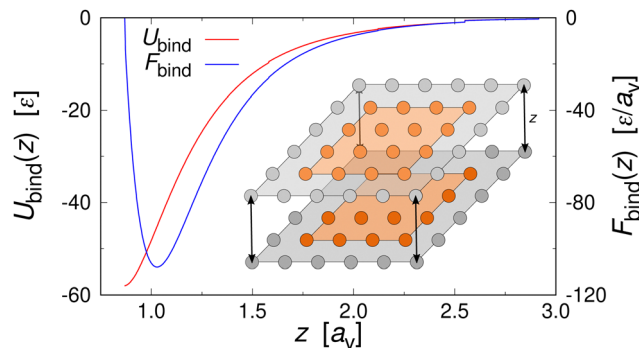
corresponding force F_{bind} plotted against the separation z between two hydrophobic faces. U_{bind} and F_{bind} are set to their minimum values of 58ε and $108\varepsilon/a_v$, respectively. The parameter $A = 10^{10}$ is chosen by matching the mean-aggregation number $\langle M \rangle$ in the KMC and MD simulations of two-patch particles at high temperature (see Section III below).

3. Shear can detach pieces from an isolated aggregate, if the hydrodynamic drag force exerted on the cubes exposed to the flow exceeds their characteristic binding force F_{bind}. We describe this event through the kernel[56]

$$K_i^{SB} = A\tau_D^{-1} \exp[-U_{bind}/(k_B T)]\frac{\xi M_i \dot{\gamma} L_i}{M_i^{2/3} F_{bind}}, \quad (6)$$

with shear rate $\dot{\gamma}$.

4. In sheared systems, the clusters collide much more frequently, which can drastically affect their aggregation and breakup behavior. We incorporate shear-induced aggregation in our KMC model through the laminar shear kernel[55]

$$K_{ij}^{SCA} = \frac{W_{ij}}{V}\dot{\gamma}(L_i + L_j)^3. \quad (7)$$

5. Conversely, clusters colliding in a sheared suspension can also fragment into smaller pieces if the kinetic energy of impact, U_{coll}, is comparable to the binding energy, U_{bind}. Assuming a perfectly inelastic collision, we estimate U_{coll} as

$$U_{coll} = \frac{m\dot{\gamma}^2}{3}\frac{M_i M_j}{M_i + M_j}(L_i/2 + L_j/2)^2. \quad (8)$$

In analogy to eqn (7), we incorporate this collision-induced breakup through the kernel

$$K_{ij}^{SCB} = \frac{1 - W_{ij}}{V}\dot{\gamma}(L_i + L_j)^3 P_{SCB} \quad (9)$$

with $P_{SCB} = \min\{1, \exp[(U_{coll} - U_{bind})/(k_B T)]\}$. In experiments and our explicit-solvent MD+MPCD simulations, the collision between two aggregates is only partially inelastic, where some fraction of U_{coll} is transferred to the surrounding solvent in form of, *e.g.*, friction or sound. This effect leads to a reduction of P_{SCB} for a given shear rate $\dot{\gamma}$, which in turn smears out the transition to the collision-dominated regime (see Section III B

below). However, once this collision-dominated regime has been reached at high $\dot{\gamma}$, the differences between the implicit- and explicit-solvent models disappear, since frictional losses *etc.* become negligible, so that $P_{SCB} = 1$.

The total number of cubes is fixed to $N = 10^4$, unless stated otherwise explicitly, and 10–100 independent simulations were performed to gather statistics for each set of parameters. We distinguish between the different patch arrangements on the cubes through the scaling exponent α (see Fig. 1), which describes the shape of the self-assembled aggregates.

III. Results

A. Equilibrium self-assembly

Fig. 5(a) shows the mean aggregation number $\langle M \rangle$ as a function of time for mixtures of two- and one-patch cubes at rest. Here, $\langle M \rangle$ is defined as $\langle M \rangle \equiv \sum_i^N M P(M)$, where $P(M)$ is the probability to find a cube in an aggregate consisting of M nanoparticles (see ref. 29 for technical details of the cluster analysis). The KMC and MD simulation results match closely when the

Fig. 5 (a) Temporal evolution of $\langle M \rangle$ in mixtures of one- and two-patch cubes (type I) at $f = 0.25$ and $f = 0.50$ from MD (solid lines) and KMC (dashed lines) simulations for $\phi = 0.112$. Data shown for temperatures $k_B T = \varepsilon$ and $k_B T = 2\varepsilon$. (b) Equilibrium $\langle M \rangle$ vs. f from KMC (lines) and MD (symbols) simulations at $\phi = 0.112$. Solid lines and filled symbols show results for $k_B T = \varepsilon$, while dashed lines and open symbols show results for $k_B T = 2\varepsilon$. The black dotted line shows the expectation value $\langle M \rangle_{urn}$ of the corresponding negative hypergeometric probability distribution. Inset: $\langle M \rangle$ vs. ϕ for type I case at $k_B T = 2\varepsilon$.

time in the KMC simulations is rescaled by a constant factor, validating the KMC model. Starting from a completely dissociated state, $\langle M \rangle = 1$ initially, the mean aggregation number increased over time and eventually reaches a plateau equilibrium value that is higher for larger f. At higher temperatures, $\langle M \rangle$ decreased and shows stronger fluctuations due to continuous aggregate breakup and reformation.

The equilibrium value of $\langle M \rangle$ increased monotonically with increasing f [Fig. 5(b)], since there were fewer one-patch cubes that can terminate cluster growth ($\langle M \rangle = 2$ at most for a pure suspension of one-patch cubes). Interestingly, the type I and type II cases exhibit almost identical $\langle M \rangle$ values, suggesting that the placement of hydrophobic patches on nanocubes has little effect on the mean aggregation number. The self-assembly behavior of these one- and two-patch cube mixtures shares similarities with the statistics problem of drawing without replacement from an urn containing two particle types with N particles in total. In this context, the probability of k successful draws (two-patch particles) until r failed draws (one-patch particles) is given by a negative hypergeometric distribution, with expectation value

$$\langle M \rangle_{urn} = \frac{rfN}{N(1-f)+1} + r \qquad (10)$$

including the r failed attempts (one-patch particles). For clusters consisting of two-patch cubes, two one-patch cubes are needed to terminate growth, so that $r = 2$. Further, for sufficiently large $N \gg 1$, eqn (10) simplifies to $\langle M \rangle_{urn} \approx 2f/(1-f) + 2$. We have plotted $\langle M \rangle_{urn}$ as a dotted line in Fig. 5, which increases similarly with f like the KMC and MD simulations, but systematically lies below the simulation results. This difference likely stems from the fact that only one particle is drawn at a time in the urn model, whereas the KMC and MD simulations allow merging events between clusters with M_i, $M_j > 1$.

For fixed f, $\langle M \rangle$ increased monotonically with increasing nanoparticle volume fraction ϕ in both KMC and MD simulations [inset of Fig. 5(b)]. This behavior can be explained by recognizing that the rate of diffusion-driven aggregation between two clusters depends on the characteristic distance between them [given by K_{ij}^{DA} in eqn (4)], while the thermal breakup rate of a cluster does not involve any other interaction partner and is thus independent of ϕ [given by K^{TB} in eqn (5)]. Notably, our previous KMC model[29] did not capture this ϕ-dependence of $\langle M \rangle$, as it did not include any cluster breakup.

At this point, we briefly discuss the effect of hydrodynamic interactions on the aggregation kinetics. To this end, we ran additional explicit-solvent simulations, using the MPCD algorithm (see Section II A for details). Fig. 6 shows the temporal evolution of $\langle M \rangle$ for two selected two-patch cases, demonstrating the excellent agreement of both methods. Here, we factored in the differences in solvent friction between the implicit- and explicit-solvent simulations by dividing the time scale through the characteristic time that a single cube needs to diffuse its own diameter, *i.e.*, $\tau_D \equiv d^2/(6D_0)$. In particular, we used $\tau_D = N_v \xi_v d^2/(6k_B T) \approx 630\tau$ for the MD simulations with a Langevin thermostat, and $\tau_D = 1.346 \times 3\pi\eta_s d^3/(6k_B T) \approx 2300\tau$
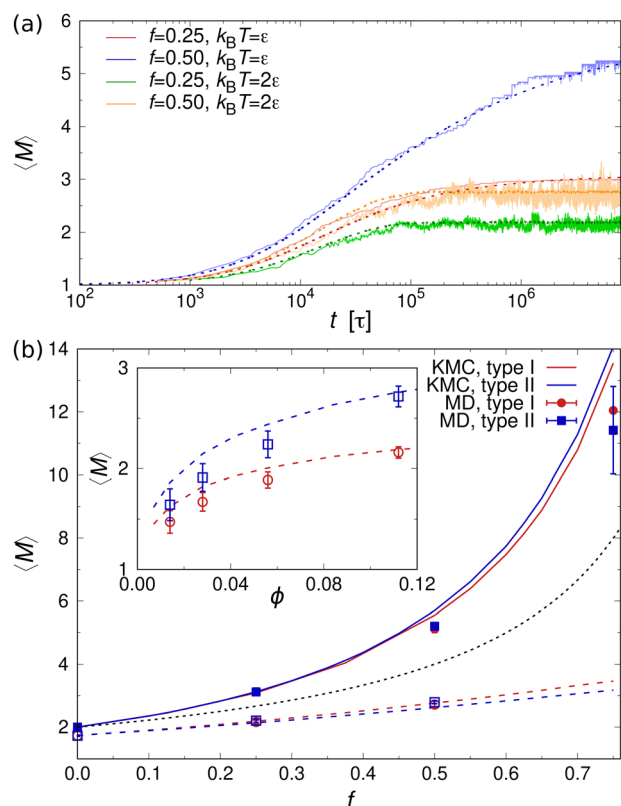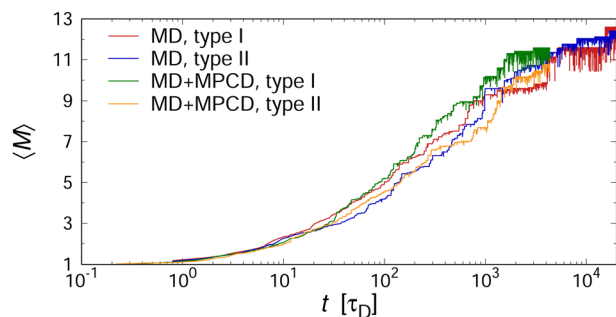
Fig. 6 $\langle M \rangle$ vs. normalized time t/τ_D in mixtures of one- and two-patch cubes at $f = 0.75$ and $\phi = 0.112$ from MD simulations without hydrodynamic interactions and MD+MPCD simulations with hydrodynamic interactions.

for the MD+MPCD simulations, where the prefactor of 1.346 accounts for the cubic shape of the colloids.[57]

Next, we examined the self-assembly behavior of mixtures containing one- and three-patch cubes at rest. The temporal evolution of the mean aggregation number $\langle M \rangle$ is plotted in Fig. 7(a) for mixtures containing three-patch cubes at fixed volume fraction $\phi = 0.112$. Comparing the self-assembly dynamics of the two- and three-patch cases [cf. Fig. 5(a) and 7(a)], we observed that the latter exhibited much slower kinetics, occurring on time scales that were more than ten orders of magnitude larger. For small $f \leq 0.2$, $\langle M \rangle$ increased monotonically until it reached its equilibrium value. For $f > 0.2$, $\langle M \rangle$ first reached an intermediate plateau, followed by a step-wise growth due to the recombination and merging of large clusters. After all of the possible clusters formed, breaking up and aggregation events typically alternated. Large clusters are, however, more prone to thermal breakup compared to smaller ones, since the probability for cluster breakup is proportional to the number of bonded hydrophobic surfaces; for example, a cluster consisting of $M_i = 20$ cubes has 19 bonded surfaces, whereas the same cubes in the form of ten dimers ($M_i = 2$) have only ten bonded surfaces in total. Therefore, two break-up events can happen consequentially for large clusters, resulting in a shorter lifetime compared to small clusters, which is reflected by the steep decline of the mean aggregation number $\langle M \rangle$ for $f > 0.2$ at late times. In principle, these smaller fragments could merge again into a larger cluster at some point, resulting in long-time fluctuations of $\langle M \rangle$ around its equilibrium value. However, we were unable to probe such time scales even with our KMC model, which underlines the challenges of equilibrating mixtures containing a large fraction of three-patch cubes.

Fig. 7(b) shows $\langle M \rangle$ as a function of the fraction f of three-patch cubes obtained from the MD and KMC simulations. Here, we included only the KMC data for $f \leq 0.2$, where $\langle M \rangle$ reached a steady plateau. Like the two-patch cubes, $\langle M \rangle$ increased monotonically with increasing f, albeit the self-assembled clusters were much larger for the three-patch case at a given f, e.g., $\langle M \rangle \approx 20$ (three-patch) vs. $\langle M \rangle \approx 2.8$ (two-patch) in KMC simulations at $f = 0.2$. To understand the larger cluster size and slower self-assembly kinetics of
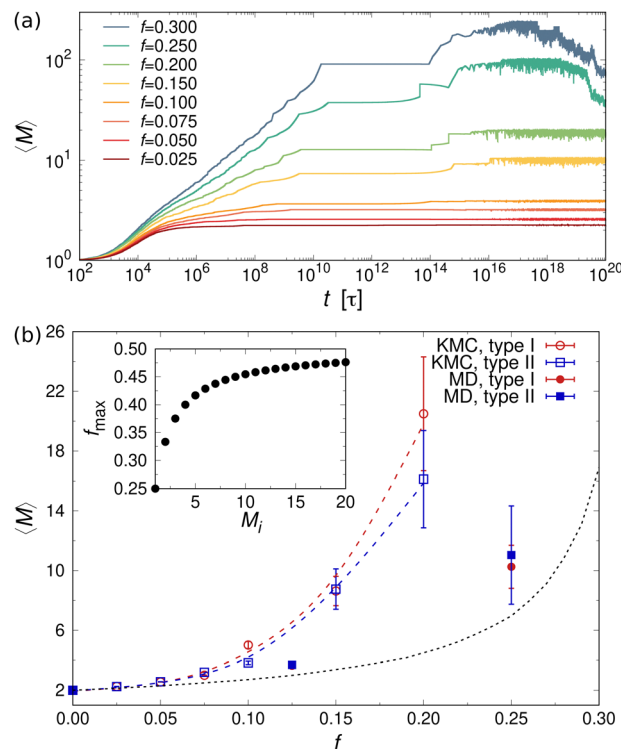

Fig. 7 (a) Temporal evolution of $\langle M \rangle$ in mixtures of one- and three-patch cubes (type II) at $\phi = 0.112$. (b) Equilibrium $\langle M \rangle$ vs. f from KMC (lines) and MD (symbols) simulations for mixtures of one- and three-patch cubes (type I) at $\phi = 0.112$ and $k_B T = \varepsilon$. The black dotted line shows the expectation value $\langle M \rangle_{\text{urn}}$. Inset: theoretical maximum value of f needed for terminating growth of a cluster consisting of M_i three-patch cubes.

three-patch cubes, it is helpful to consider the conditions for terminating cluster growth: while aggregates composed of two-patch cubes need only two one-patch cubes to stop cluster growth, irrespective of their aggregation number M_i, a cluster consisting of M_i three-patch cubes requires $M_i + 2$ one-patch cubes to prevent further aggregation. Hence, to achieve a stable suspension of finite-sized aggregates, the fraction of multi-patch nanocubes cannot exceed $f_{\text{max}} \equiv M_i/(2M_i + 2)$, which approaches $f_{\text{max}} \approx 1/2$ for large M_i [see inset of Fig. 7(b)]. In addition, the one-patch cubes must adsorb successively to the exposed hydrophobic surfaces of a three-patch cube, which has a probability of roughly $(1 - f)^2$ for $M_i \geq 2$ to first approximation. Since the criteria for terminating the growth of a cluster depend on its size and composition, it is difficult to approximate the aggregation behavior using an analytically tractable urn model [cf. eqn (10) for the two-patch case]. We can, however, numerically compute $\langle M \rangle_{\text{urn}}$, which is shown as a dotted line in Fig. 7(b).

Finally, we conducted a visual examination of the MD trajectories to assess the emergence of ordered superstructures; hard cubic nanoparticles are expected to undergo a first-order transition from a fluid to a solid phase around packing fractions of $\phi_f \approx 0.5$, where the (crystal) structure depends on the faceting and sharpness of the nanoparticles.[23,58,59] Our simulations were limited to much smaller volume fractions $\phi \leq 0.112$,

and thus remained in the fluid phase. The rod-like clusters formed by type I two-patch cubes have the potential to exhibit nematic liquid crystal behavior if the increase in positional entropy outweighs the corresponding decrease in orientational entropy.[60] However, our MD simulations did not reveal any evidence of nematic ordering. This observation aligns with previous simulations of hard spherocylinders:[61] based on those simulations, we expect the isotropic-nematic transition near $\phi_{\text{in}} \approx 0.3$ for our longest rod-like clusters, which have an average aspect ratio of roughly $\langle L/d \rangle = \langle M \rangle \approx 10$ [see Fig. 5(b)]. Thus, achieving ordered superstructures would necessitate either larger clusters and/or higher volume fractions, which will be the subject of future work.

B. Shear-induced aggregation and breakup

Nanoparticles in sheared suspensions experience many more collisions among them compared to quiescent suspensions, which can lead to the enhanced growth or breakup of the aggregates depending on the flow conditions and particle interactions.[6,8,55,62,63] In addition, shear flow can deform the aggregates, which can facilitate the formation of additional interparticle bonds. To characterize the strength of the shear flow, we introduce the Péclet number

$$\text{Pe} \equiv \frac{\dot{\gamma} d^2}{D_0}, \tag{11}$$

which is the ratio between the rate of advection and the rate of diffusion for a single cubic particle. Another useful dimensionless quantity for characterizing the flow regime is the Reynolds number $\text{Re} \equiv \rho_s m_s \dot{\gamma} L_i^2 / \eta_s$, which is defined as the ratio of the inertial and viscous forces acting on a sheared aggregate. For a rod-like cluster consisting of $M_i = 10$ cubes suspended in the MPCD fluid, the typical Reynolds numbers lie between $0.02 \lesssim \text{Re} \lesssim 20$ for $0.1 \lesssim \text{Pe} \lesssim 100$, so that inertial effects can become relevant.

Fig. 8(a) shows the time evolution of $\langle M \rangle$ for a mixture of one- and two-patch cubes at different values of Pe. The data confirm that the cubes aggregate much earlier in the sheared systems, as expected from the advective transport. However, the steady-state $\langle M \rangle$ is significantly smaller in the sheared suspensions compared to the systems at rest. For example, at $\text{Pe} = 10^2$, the majority of aggregates are dimers, whereas at rest there are many rod-shaped aggregates consisting of more than ten cubes. These trends apply to all investigated ϕ and f, with only minor quantitative differences between the type I and type II patch arrangements, as shown in Fig. 8(b).

For validating the KMC results for sheared suspensions, we performed non-equilibrium MD+MPCD simulations at $\phi = 0.112$ and $f = 0.75$. The resulting steady-state values of $\langle M \rangle$ are shown in Fig. 8(c), which qualitatively exhibit the same monotonic decrease of $\langle M \rangle$ with increasing Pe as the KMC simulations, indicative of shear-induced cluster breakup. There are, however, some quantitative differences at intermediate Péclet numbers $1 \lesssim \text{Pe} \lesssim 10$, where we find a broader transition regime in the MD simulations compared to the KMC calculations. This effect likely stems from the fact that
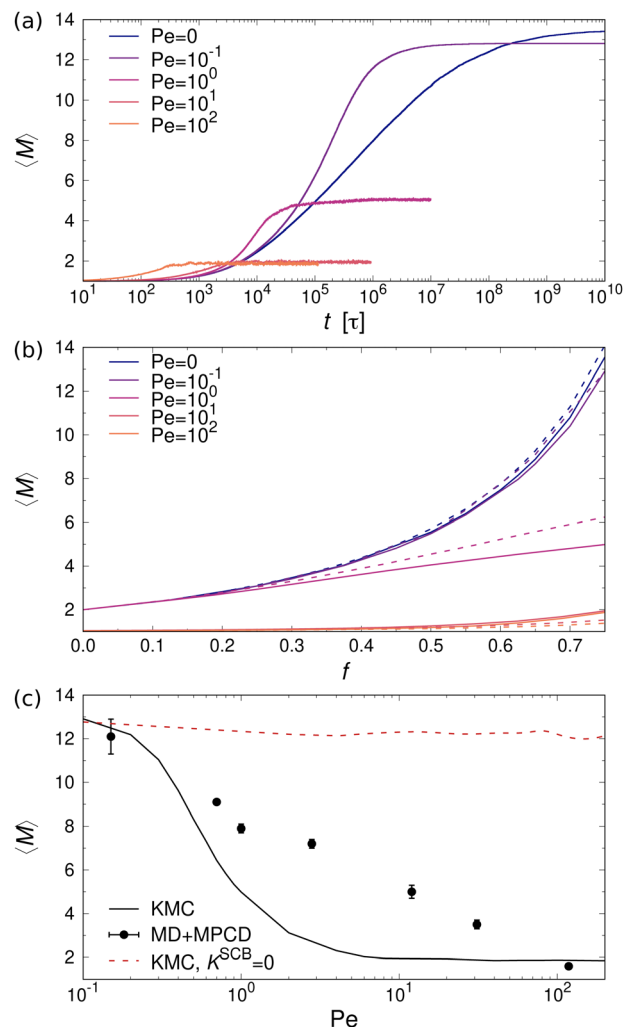

Fig. 8 (a) Temporal evolution of $\langle M \rangle$ in mixtures of one- and two-patch cubes (type I) from KMC simulations at $f = 0.75$ and $\phi = 0.112$. (b) Steady-state $\langle M \rangle$ *vs.* f for type I (solid lines) and type II (dashed lines) two-patch cubes. (c) Results from KMC (lines) and non-equilibrium MD+MPCD simulations (symbols) of two-patch cubes (type I) at $f = 0.75$ and $\phi = 0.112$. The dashed red line shows results from KMC simulations with $K_{ij}^{\text{SCB}} = 0$.

some fraction of the collisional energy is transferred to the surrounding solvent, so that the collisions between aggregates cannot be regarded as perfectly inelastic, which is assumed in our KMC model (see Section II A). To test this hypothesis, we performed additional KMC calculations where we turned off the collision-induced breakup of aggregates by setting $K_{ij}^{\text{SCB}} = 0$. In that case, the aggregates were much more stable under shear so that the mean aggregation number $\langle M \rangle$ from the KMC simulations lied consistently above the one from the MD+MPCD simulations, as indicated by the red dashed line in Fig. 8(c). Hence, the the shear-induced collision between aggregates plays a crucial role for their breakup, but this effect is somewhat overemphasized in our KMC model, which assumes perfectly inelastic collisions between them.

In order to gain insight into the physical mechanisms driving the assembly under shear, we examined how the rate
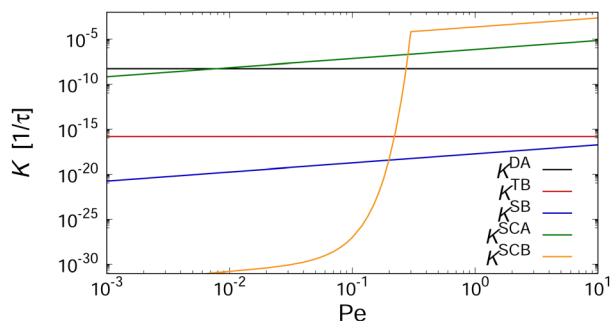
Fig. 9 Rates for diffusion-driven aggregation K_{ij}^{DA}, thermally-induced breakup K^{TB}, shear-induced breakup K_i^{SB}, shear-induced collisional aggregation K_{ij}^{SCA}, and shear-induced collisional breakup K_{ij}^{SCB} vs. Péclet number. Data shown for a pair of clusters with $M_i = M_j = 4$, consisting of one one-patch and three two-patch cubes (type I), in a sheared suspension with $\phi = 0.112$ and $k_BT = \varepsilon$.

kernels K change as the Péclet number increases. As an example, we have plotted in Fig. 9 these dependencies for the kernels describing the interactions between two aggregates with $M_i = M_j = 4$ at $k_BT = \varepsilon$. The kernels describing diffusion-driven aggregation, K^{DA}, and thermal breakup, K^{TB}, are independent of the applied shear rate $\dot{\gamma}$ [cf. eqn (4) and (5)], with $K^{DA}/K^{TB} \sim 10^7$ at $k_BT = \varepsilon$ so that aggregation is virtually irreversible. At elevated temperature $k_BT = 2\varepsilon$, this ratio decreases drastically to $K^{DA}/K^{TB} \sim 10^{-5}$, thus greatly favoring the dissociation of the aggregates (cf. Fig. 5).

To gauge the relevance of shear for the growth of the aggregates, consider the ratio K_{ij}^{SCA}/K_{ij}^{DA}, which becomes larger than unity when

$$\text{Pe} \geq \frac{M_i^{-1} + M_j^{-1}}{(M_i + M_j)^{2\alpha}}. \tag{12}$$

Thus, the shear-induced collision of clusters becomes the dominant aggregation mechanism already at rather small Péclet numbers, i.e., $\text{Pe} \geq 2^{1/3}$ for the "worst case" of two three-patch cubes with type II patch arrangement ($M_i = M_j = 1$, $\alpha = 1/3$). This threshold quickly drops with increasing aggregate size, which explains the rapid increase in $\langle M \rangle$ in the sheared systems.

To understand why the steady-state average cluster size decreases with increasing Pe (see Fig. 8), it is helpful to regard the breakup kernels K_i^{TB}, K_i^{SB}, and K_{ij}^{SCB}. The frequency of shear-induced breakup of a single aggregate increases linearly with increasing Péclet number Pe, and it should surpass the rate of thermal breakup when $K_i^{SB}/K_i^{TB} \geq 1$. Comparing eqn (5) and (6) then yields

$$\text{Pe} \geq \frac{dF_{bind}}{k_BTM_i^{(1/3+\alpha)}}. \tag{13}$$

For the parameters used in this work, i.e., $d = 5a_v$, $F_{bind} = 108\varepsilon/a_v$ and $k_BT \sim \varepsilon$, the shear forces exerted on a single rod-shaped aggregate with $M_i = 4$ become comparable to the thermal forces at $\text{Pe} \geq 85$, while the threshold decreases to $\text{Pe} \geq 10$ for a longer rod with $M_i = 20$.

If the suspension is not infinitely dilute, then collisions between clusters can also lead to the breakup of clusters. Such cooperative effects should become relevant when $K_{ij}^{SCB}/K_{ij}^{SCA} \geq 1$. Combining eqn (7) and (9) leads to

$$(W_{ij}^{-1} - 1)P_{SCB} \geq 1, \tag{14}$$

which holds as soon as $P_{SCB} \approx 1$, since $(W_{ij}^{-1} - 1) > 1$ for all investigated cases. This condition is fulfilled when the kinetic energy of impact $U_{coll} \propto \text{Pe}^2$ equals or exceeds the typical binding energy between aggregated cubes, U_{bind} (see Section II B). From Fig. 9 we see that the overall contribution of K_{ij}^{SCB} is negligible for small Péclet numbers, but then suddenly jumps up near $\text{Pe} \sim 10^{-1}$ and surpasses all other rate kernels for larger Pe. For collisions between larger clusters, this transition shifts to smaller Péclet numbers, since U_{coll} scales roughly as $U_{coll} \propto (L_i + L_j)^2$, while U_{bind} is independent of cluster size. Fig. 9 also confirms the Pe-independent ratio $K_{ij}^{SCB}/K_{ij}^{SCA} > 1$ at sufficiently high Péclet numbers, as expected from eqn (14). The importance of collective collisions for the shear-induced breakup of clusters is consistent with our MD simulations, where we observed a distinct decrease of $\langle M \rangle$ already at $\text{Pe} = 1$ in sheared suspensions with $\phi = 0.112$ [see Fig. 8(c)], whereas ultradilute suspensions of rod-shaped clusters ($M_i = 4$) remained stable under shear at $\text{Pe} = 27$ but broke up at $\text{Pe} = 198$.

IV. Conclusions

We employed a combination of molecular dynamics (MD) and rejection-free Kinetic Monte Carlo (KMC) simulations to investigate the self-assembly of amphiphilic nanocubes, which can be regarded as coarse-grained models for folded proteins[36–38] or DNA-functionalized nanoparticles,[30,64] as schematically illustrated in Fig. 10. We simulated suspensions under shear and at rest, focusing on volume fractions below the freezing transitions of hard cubes. We systematically varied
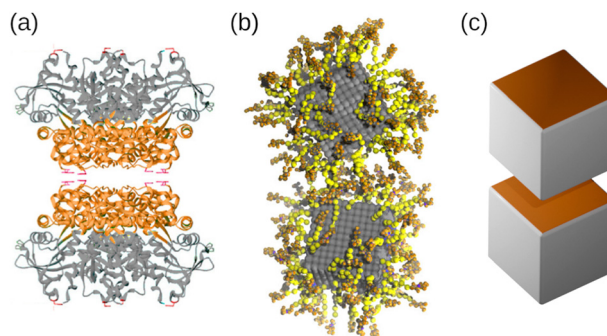

Fig. 10 (a) Schematic of a pair of cube-shaped L-rhamnulose-1-phosphate proteins with directional interactions. The "head" and "tail" regions have been colored orange and grey, respectively. (b) Simulation snapshot of gold nanoparticles (grey) coated with single-stranded DNA, where spacer and linker beads have been colored yellow and orange, respectively. (c) Rendering of two patchy nanocubes. (a) Reprinted (adapted) with permission from ref. 38. Copyright 2021 American Chemical Society. (b) Reproduced from ref. 30. Copyright 2023 AIP Publishing LLC.

the number and arrangement of hydrophobic faces on the cubes, and always included a fraction of one-patch cubes to limit growth into finite-sized aggregates. This strategy allowed the assembly into superstructures that are unattainable for spherical particles with isotropic interactions, such as elongated rods and fractal objects, depending on the number and placement of hydrophobic faces. For weak hydrophobic interactions (or high temperatures), the nanocubes continuously aggregated and dissociated from each other, resulting in small aggregates of only few nanocubes. For more hydrophobic interactions (or lower temperatures), the aggregation essentially became irreversible, so that the clusters grew continuously until all hydrophobic surfaces were covered by one-patch cubes. Mixtures containing three-patch cubes exhibited extremely slow self-assembly kinetics caused by the gradual recombination of the aggregates, highlighting the challenge of equilibrating such systems. In all investigated cases, we found that the final aggregate size increased distinctly as the fraction of multi-patch cubes in the mixtures was increased. The equilibrium results from MD and KMC were in quantitative agreement for the two-patch systems, whereas the three-patch cubes self-assembled into systematically smaller clusters in the MD simulations, likely due to finite-size effects and slow aggregation kinetics. Finally, we demonstrated that hydrodynamic interactions do not have a significant impact on the aggregation kinetics in quiescent suspensions.

In sheared suspensions, the advective motion of the nanocubes led to faster aggregation compared to the diffusion-driven self-assembly at rest, but the steady-state average cluster size decreased with increasing shear rate (or Péclet number). We rationalize this behavior by comparing the magnitudes of the relevant rate kernels in the KMC simulations, finding that the shear-induced breakup due to collisions between aggregates becomes the dominant event at high Péclet numbers. For the sheared suspensions, the results of the MD and KMC simulations were in semi-quantitative agreement, and we attribute the differences between the two approaches primarily to the approximation of perfectly inelastic collisions in the KMC model.

The overall good agreement between our various simulation methods demonstrates that the self-assembly behavior of amphiphilic cubes is rather robust and not model-specific. In addition, the general trends that were observed in quiescent and sheared suspensions should be transferable to a wide range of nanoparticles with similar anisotropic interactions, such as rod-shaped Janus particles. The patchy nanocubes also share interesting conceptual similarities with homopolymers in solution, e.g., the self-assembly into more compact aggregates with increasing number of hydrophobic surfaces is akin to the coil-globule transition of homopolymers with decreasing solvent quality.[52] There are, however, also notable differences, such as the (reversible) shear-induced dissociation of nanocube clusters into small fragments, which is impossible for homopolymer dispersions. Our complementary modeling approach, combining KMC for rapid parameter space exploration with MD for microscopic analysis, is highly promising for systematically studying the effect of various particle compositions, shapes, and sizes. Further, by combining our model with machine learning methods such as evolutionary algorithms,[65,66] it can also be used to address the inverse problem, namely identifying and optimizing the nanoparticle properties for achieving desired superstructures.

Conflicts of interest

There are no conflicts to declare.

Acknowledgements

References

1 M. Antonietti and C. Göltner, Angew. Chem., Int. Ed. Engl., 1997, **36**, 910–928.

2 A. B. Pawar and I. Kretzschmar, Macromol. Rapid Commun., 2010, **31**, 150–168.

3 S. C. Glotzer and M. J. Solomon, Nat. Mater., 2007, **6**, 557–562.

4 W. Li, H. Palis, R. Mérindol, J. Majimel, S. Ravaine and E. Duguet, Chem. Soc. Rev., 2020, **49**, 1955–1976.

5 F. Sciortino, A. Giacometti and G. Pastore, Phys. Rev. Lett., 2009, **103**, 237801.

6 E. Bianchi, A. Z. Panagiotopoulos and A. Nikoubashman, Soft Matter, 2015, **11**, 3767.

7 Y. Kobayashi and N. Arai, Soft Matter, 2016, **12**, 378–385.

8 Y. Kobayashi, N. Arai and A. Nikoubashman, Soft Matter, 2020, **16**, 476–486.

9 E. Bianchi, J. Largo, P. Tartaglia, E. Zaccarelli and F. Sciortino, Phys. Rev. Lett., 2006, **97**, 168301.

10 F. Sciortino and E. Zaccarelli, Curr. Opin. Colloid Interface Sci., 2017, **30**, 90–96.

11 L.-T.-C. Tran, S. Lesieur and V. Faivre, Expert Opin. Drug Delivery, 2014, **11**, 1061–1074.

12 H. Su, C.-A. Hurd Price, L. Jing, Q. Tian, J. Liu and K. Qian, Mater. Today Bio, 2019, **4**, 100033.

13 L. C. Bradley, W.-H. Chen, K. J. Stebe and D. Lee, Curr. Opin. Colloid Interface Sci., 2017, **30**, 25–33.

14 T. I. Morozova and A. Nikoubashman, Langmuir, 2019, **35**, 16907.

15 T. I. Morozova, V. E. Lee, N. Bizmark, S. S. Datta, R. K. Prud'homme, A. Nikoubashman and R. D. Priestley, ACS Cent. Sci., 2020, **6**, 166.

16 E. L. Correia, N. Brown and S. Razavi, Nanomater., 2021, **11**, 374.

17 A. Kirillova, C. Schliebe, G. Stoychev, A. Jakob, H. Lang and A. Synytska, ACS Appl. Mater. Interfaces, 2015, **7**, 21218–21225.

18 C. Marschelke, A. Fery and A. Synytska, *Colloid Polym. Sci.*, 2020, **298**, 841–865.

19 M. W. Beijerinck, *Verh. K. Akad. Wet. Amsterdam, Afd. Natuurkd*, 1898, **5**, 3–21.

20 F. C. Bawden, N. W. Pirie, J. D. Bernal and I. Fankuchen, *Nature*, 1936, **138**, 1051.

21 F. M. van der Kooij, K. Kassapidou and H. N. W. Lekkerkerker, *Nature*, 2000, **406**, 868–871.

22 B. S. John, A. Stroock and F. A. Escobedo, *J. Chem. Phys.*, 2004, **120**, 9383.

23 U. Agarwal and F. A. Escobedo, *Nat. Mater.*, 2011, **10**, 230–235.

24 P. F. Damasceno, M. Engel and S. C. Glotzer, *Science*, 2012, **337**, 453–457.

25 F. Smallenburg, L. Filion, M. Marechal and M. Dijkstra, *Proc. Natl. Acad. Sci. U. S. A.*, 2012, **109**, 17886–17890.

26 S.-B. Wang, Y.-L. Min and S.-H. Yu, *J. Phys. Chem. C*, 2007, **111**, 3551–3554.

27 M. Mayer, A. M. Steiner, F. Röder, P. Formanek, T. A. F. König and A. Fery, *Angew. Chem., Int. Ed.*, 2017, **56**, 15866–15870.

28 S. Toso, D. Baranov and L. Manna, *Acc. Chem. Res.*, 2021, **54**, 498–508.

29 Y. Kobayashi and A. Nikoubashman, *Langmuir*, 2022, **38**, 10642–10648.

30 Y. Zhang, G. Giunta, H. Liang and M. Dijkstra, *J. Chem. Phys.*, 2023, **158**, 184902.

31 B. Rusen Argun and A. Statt, *arXiv*, 2023, preprint, arXiv:2305.05453, DOI: **10.48550/arXiv.2305.05453**.

32 P. W. K. Rothemund, *Nature*, 2006, **440**, 297–302.

33 N. C. Seeman and H. F. Sleiman, *Nat. Rev. Mater.*, 2017, **3**, 17068.

34 S. Dey, C. Fan, K. V. Gothelf, J. Li, C. Lin, L. Liu, N. Liu, M. A. D. Nijenhuis, B. Saccà, F. C. Simmel, H. Yan and P. Zhan, *Nat. Rev. Dis. Primers*, 2021, **1**, 13.

35 M. B. Scheible, L. L. Ong, J. B. Woehrstein, R. Jungmann, P. Yin and F. C. Simmel, *Small*, 2015, **11**, 5200–5205.

36 H. Liu, S. K. Kumar and F. Sciortino, *J. Chem. Phys.*, 2007, **127**, 084902.

37 J. J. McManus, P. Charbonneau, E. Zaccarelli and N. Asherie, *Curr. Opin. Colloid Interface Sci.*, 2016, **22**, 73–79.

38 M. Du, K. Zhou, R. Yu, Y. Zhai, G. Chen and Q. Wang, *Nano Lett.*, 2021, **21**, 1749–1757.

39 Y. Ma, W. Li, E. C. Cho, Z. Li, T. Yu, J. Zeng, Z. Xie and Y. Xia, *ACS Nano*, 2010, **4**, 6725–6734.

40 J. R. Royer, G. L. Burton, D. L. Blair and S. D. Hudson, *Soft Matter*, 2015, **11**, 5656–5665.

41 S. H. Sajjadi and E. K. Goharshadi, *J. Environ. Chem. Eng.*, 2017, **5**, 1096–1106.

42 W. Humphrey, A. Dalke and K. Schulten, *J. Mol. Graphics*, 1996, **14**, 33–38.

43 Y. M. Wani, P. G. Kovakas, A. Nikoubashman and M. P. Howard, *J. Chem. Phys.*, 2022, **156**, 024901.

44 S. Poblete, A. Wysocki, G. Gompper and R. G. Winkler, *Phys. Rev. E: Stat., Nonlinear, Soft Matter Phys.*, 2014, **90**, 033314.

45 J. D. Weeks, D. Chandler and H. C. Andersen, *J. Chem. Phys.*, 1971, **54**, 5237–5247.

46 A. Malevanets and R. Kapral, *J. Chem. Phys.*, 1999, **110**, 8605–8613.

47 G. Gompper, T. Ihle, D. Kroll and R. G. Winkler, *Adv. Polym. Sci.*, 2009, **221**, 1–87.

48 M. P. Howard, A. Nikoubashman and J. C. Palmer, *Curr. Opin. Chem. Eng.*, 2019, **23**, 34.

49 Y. Kobayashi, N. Arai and A. Nikoubashman, *Langmuir*, 2020, **36**, 14214–14223.

50 F. Müller-Plathe, *Phys. Rev. E: Stat. Phys., Plasmas, Fluids, Relat. Interdiscip. Top.*, 1999, **59**, 4894–4898.

51 J. A. Anderson, J. Glaser and S. C. Glotzer, *Comput. Mater. Sci.*, 2020, **173**, 109363.

52 M. Rubinstein and R. H. Colby, *Polymer Physics*, Oxford University Press, Oxford, 2003.

53 M. M. Tirado, C. López Martínez and J. G. de la Torre, *J. Chem. Phys.*, 1984, **81**, 2047–2052.

54 M. von Smoluchowski, *Phys. Zeit*, 1916, **17**, 557–585.

55 M. von Smoluchowski, *Z. Physik. Chem.*, 1918, **92**, 129–168.

56 M. Icardi, N. Di Pasquale, E. Crevacore, D. Marchisio and M. U. Babler, *Transp. Porous Media*, 2023, **146**, 197–222.

57 J. Happel and H. Brenner, *Low Reynolds Number Hydrodynamics: with special applications to particulate media*, Springer, 1983.

58 R. Ni, A. P. Gantapara, J. de Graaf, R. van Roij and M. Dijkstra, *Soft Matter*, 2012, **8**, 8826–8834.

59 G. van Anders, N. K. Ahmed, R. Smith, M. Engel and S. C. Glotzer, *ACS Nano*, 2014, **8**, 931–940.

60 L. Onsager, *Ann. N. Y. Acad. Sci.*, 1949, **51**, 627–659.

61 P. Bolhuis and D. Frenkel, *J. Chem. Phys.*, 1997, **106**, 666.

62 V. Oles, *J. Colloid Interface Sci.*, 1992, **154**, 351–358.

63 A. Zaccone, D. Gentili, H. Wu, M. Morbidelli and E. Del Gado, *Phys. Rev. Lett.*, 2011, **106**, 138301.

64 M. N. O'Brien, M. Girard, H.-X. Lin and C. A. Mirkin, *Proc. Natl. Acad. Sci. U. S. A.*, 2016, **113**, 10485–10490.

65 A. R. Oganov and C. W. Glass, *J. Chem. Phys.*, 2006, **124**, 244704.

66 N. D. Petsev, A. Nikoubashman, F. Latinwo, F. H. Stillinger and P. G. Debenedetti, *J. Phys. Chem. B*, 2022, **126**, 7771–7780.